AIAA JOURNAL
Vol. 46, No. 2, February 2008

Supersonic Boundary Layers with Periodic Surface Roughness

Isaac W. Ekoto*
Sandia National Laboratories, Livermore, California 94551-9056
Rodney D. W. Bowersox†
Texas A&M University, College Station, Texas 77843-3141
Thomas Beutner‡
Defense Advanced Research Projects Agency, Arlington, Virginia 22203-1714
and
Larry Goss§
Innovative Scientific Solutions Inc., Dayton, Ohio 45440-3638

DOI: 10.2514/1.31729

In the present study, the effects of large-scale periodic surface roughness on a high-speed ($M = 2.86$), high Reynolds number ($Re_\theta \approx 60,000$), supersonic turbulent boundary layer was examined. Two roughness topologies (square and diamond) were compared with an aerodynamically smooth wall. The measurements included planar contours of the mean and fluctuating velocity, pitot pressure profiles, pressure-sensitive paint, and schlieren photography. The local strain-rate distortion parameters for the square roughness pattern were small (~ -0.01), and the mean and turbulent flow properties followed the canonical rough-wall boundary-layer trends. The diamond-shaped roughness topology produced a pattern of attached oblique shocks and expansion waves that led to strong distortion parameters. The distortions varied from −0.3 to 0.4 across the roughness elements, which resulted in localized extra turbulence production that generated large periodic variations in the turbulence levels across individual roughness elements that spanned the boundary-layer thickness; for example, the Reynolds shear stress varied by ∼100%. This result demonstrated a mechanism for altering the turbulence in supersonic boundary layers.

Nomenclature

a	=	roughness-element width
b	=	roughness-element length
d	=	distortion parameter defined as the extra-strain rate normalized by $\mathrm{d}U/\mathrm{d}y$.
I	=	impulse parameter
k	=	roughness-element height
M	=	Mach number
p	=	pressure
$\bar{p}_w$	=	area-averaged surface pressure
Δp_w	=	axial wall pressure variation $[(p_w - \bar{p}_w)/\bar{p}_w]$
P_{ij}	=	turbulent-stress production $(\tau^T_{jk}U_{i,k} + \tau^T_{ik}U_{j,k})$
Re	=	Reynolds number $(\rho UL/\mu)$
T	=	temperature
u, v	=	instantaneous velocity components
U, V	=	mean velocity components
U_{ref}	=	reference velocity (625 m/s)
u^*	=	friction velocity $(\tau_w/\rho_w)^{1/2}$
$\Delta u^+_{\mathrm{eff}}$	=	defect velocity $[(U_{\mathrm{eff}} - U_{e,\mathrm{eff}})/u^*]$
w	=	space between roughness elements
x, y, z	=	Cartesian coordinates (axial, wall normal, and lateral directions, respectively)
δ	=	boundary-layer thickness
δ^*	=	boundary-layer displacement thickness
δ_{ref}	=	reference boundary-layer thickness (10.0 mm)
λ	=	roughness-element spacing wavelength
θ	=	momentum thickness
μ	=	dynamic viscosity
ρ	=	instantaneous density
$\bar{\rho}$	=	mean (time) density
τ	=	shear stress

Subscripts

e	=	boundary-layer edge condition
eff	=	van Driest II scaled velocity
i, j, k	=	Cartesian indices
ref	=	reference condition
s	=	sand grain
w	=	wall
0	=	total condition

Superscripts

T	=	turbulent
$'$	=	Reynolds fluctuation
$+$	=	inner-variable scaled component $[\rho_w u^*(\_)/\mu_w]$

Received 20 April 2007; revision received 18 September 2007; accepted for publication 19 September 2007.

*Postdoctoral Student, Combustion Research Facility. Member AIAA.
†Professor, Aerospace Engineering, H. R. Bright Building. Associate Fellow AIAA.
‡Program Manager, 3701 North Fairfax Drive. Associate Fellow AIAA.
§President, 2766 Indian Ripple Road. Associate Fellow AIAA.

I. Introduction

IMPROVED understanding of the fundamental physics associated with turbulent supersonic boundary layers with surface roughness has many engineering applications, including reentry vehicle thermal protection and internal aeropropulsive flows. An extensive database of the mean and turbulent flow properties exists for low-speed rough-wall flows [1–8], and the associated flow scaling has provided the foundation for turbulence models suitable for low-speed zero-pressure-gradient flow (Wilcox [9]). These studies have shown that surface roughness has a direct effect on the inner region of the law of the wall and is often described by the single roughness Reynolds number k_s^+ parameter. Three roughness regimes have been identified for low-speed flow: aerodynamically smooth ($k_s^+ < 4$–5), transitional (4–$5 < k_s^+ < 60$–70), and fully rough ($k_s^+ > 60$–70). Nikuradse [1] demonstrated that sand-grain-generated roughness increased the velocity defect and skin friction and shifted the

logarithmic region of the law of the wall downward. However, the same defect-law scaling was found to hold for rough and smooth walls. The amount of downward shift of the logarithmic region of the boundary layer was shown to be a function of k^+. Schlichting [8] introduced the concept of equivalent sand-grain roughness k_s^+ to correlate any surface roughness to the equivalent Nikuradse sand-grain roughness for comparison. Equivalent sand-grain roughness does not include any characterization of the roughness topology. Investigations of the influence of the roughness geometry have been performed [3–7]. However, a general description has not been developed. The basic trend in the turbulence results of Corrsin and Kistler [2] for a fully rough flow was that the axial turbulence-intensity levels increased by about 30–40% and the Reynolds shear stresses nearly doubled. These data imply that roughness significantly alters the production and dissipation of turbulence. Grass [10] concluded that a different dominant mode of near-wall instability "might prevail" for rough walls.

For high-speed flow, Goddard [11] and Berg [12] found that for Mach numbers between 0.7–6.0, the shift in the law-of-the-wall velocity profile followed the incompressible case when the van Driest II compressibility transformation was used. Liepmann and Goddard [13] conjectured that for fully rough flow, the wall shear force is primarily the result of the drag on the roughness elements. Based on this argument, they showed that the ratio of compressible to incompressible skin friction is equal to the wall-to-freestream density ratio. The force balance data of Goddard [11] confirmed the Liepmann and Goddard [13] skin friction correlation over a Mach number range of 0.7–4.54. Young [14] developed a reference temperature method to extend the Liepmann and Goddard [13] relation to flow with heat transfer. Focusing more on the turbulent field, Latin and Bowersox [15] found that at Mach 2.8, smaller roughness elements increased the skin frictional losses more than the boundary-layer turbulence levels. However, as the roughness height was increased, the turbulence production relative to the frictional losses increased. They also showed that the kinematic statistical turbulent flow properties for the sand-grain test cases collapsed onto a single curve when scaled with outer-flow variables. Machined patterns, however, did not collapse, indicating that turbulence production mechanisms are dependent on the roughness topology. Also, the statistical fluctuating properties with an explicit thermodynamic dependence did not collapse when scaled by local mean quantities and increased almost linearly with k_s^+. Latin and Bowersox [15] found that the roughness elements significantly altered the spectral content of the turbulence, and it was inferred that the turbulent energy was shifted down from larger to smaller scales.

Also relevant to the present study is the body of knowledge concerning the effects of pressure gradients and streamline curvature in supersonic boundary turbulent layers [16–23]. In summary, the effects of favorable pressure gradients on turbulent quantities have been found to reduce turbulence levels, whereas the opposite is true for adverse pressure gradients. In boundary layers, the distortion d is defined as the ratio of the secondary strain rates to the primary velocity gradient normal to the wall. The distortion is generally considered mild if $d < 0.01$ and strong if $d > 0.1$ [16]. It has been repeatedly observed [20–23] that favorable pressure gradients and convex wall curvature have a stabilizing effect, with axial turbulence intensities observed to decrease by up to 90% and turbulent shear stress by as much 75% [20]. Streamline-driven favorable pressure gradients have also been shown to produce negative Reynolds shear stresses in the outer half of the boundary layer, whereas the principle strain rate remained positive. Arnette et al. [21] termed this observation an "apparent reverse transition," in which the normal energy transfer from the mean flow to the turbulence had been reversed. Luker et al. [20] observed that the associated extra production terms due to the induced strain rates resulted in a negative overall turbulence production in the same region of the boundary layer. The collective data indicated that the favorable pressure gradients were disintegrating the large-scale eddies into smaller ones. This redistribution of energy increased the amount of turbulent energy available for dissipation by the flow, which in turn had the observed stabilizing effect on the boundary layer.

The objective of the present study was to improve our basic understanding of how local flow distortions generated by periodic surface roughness topologies alter the mean and turbulent flow structure of supersonic boundary layers. This understanding has the potential to lead to methods for local flow tailoring or control. Specifically, two roughness topologies with significantly different localized flow distortions were compared. The heights of the roughness elements were chosen to produce significant roughness effects: that is, $k_s^+ \sim 100$. Experimental examination of the mean and turbulent boundary-layer flow structure was performed, in which the local flow over the roughness elements was resolved. The goals of the experiments were 1) quantification of effects of the local flow distortion on the mean flow properties, turbulent statistics, and turbulence production and 2) characterization of the effects of surface topology on the accepted scaling.

II. Facilities and Diagnostic Test Equipment

A. Wind-Tunnel Description

The experiments were performed in a supersonic wind tunnel located at Texas A&M University. A schematic of the wind tunnel is given in Fig. 1. This blowdown facility had a freestream Mach number of 2.86 with a $\pm 1.0\%$ variation across the test section. The nozzle exit dimensions were 7.62 by 7.62 cm. The stagnation pressure and temperature were set to 690 kPa ($\pm 5.0\%$) and 313 K ($\pm 3.5\%$), respectively. At the operating stagnation temperature, the adiabatic wall temperature was approximately equal to the ambient temperature in the laboratory, which, when coupled with the relatively low thermal conductivity of the Plexiglas floors in the tunnel, resulted in minimal heat transfer during the 90-s wind-tunnel runs. The nominal wall temperature and density were $T_w = 292$ K and $\rho_w = 0.277$ kg/m^3.

A pitot probe with an Omega brand PX303 0–690-kPa pressure transducer ($\pm 0.25\%$ full-scale accuracy) was used to monitor the stagnation pressure within the settling chamber. The total temperature was measured using an Omega brand JQSS thermocouple amplified by an OMNI AMP-IV thermocouple amplifier. Tunnel static pressure was measured with five Omega brand PX303 0–103-kPa pressure transducers ($\pm 0.25\%$ full-scale accuracy). Data from the pressure transducers and thermocouples were collected by a Keithley brand KPCI-3110 data acquisition board with a sampling rate of 1.25 M/s. The board had 12-bit resolution with 16 differential channels.

The measurements took place in the floor boundary layer of the wind tunnel. The test section was located just downstream of the nozzle exit (see Fig. 1). The wind tunnel uses a half-nozzle block to achieve the Mach-3 flow, as indicated by the bolt pattern shown schematically in Fig. 1. Because of the half-block design, the floor boundary layer experienced 20.5 cm of constant pressure flow in the

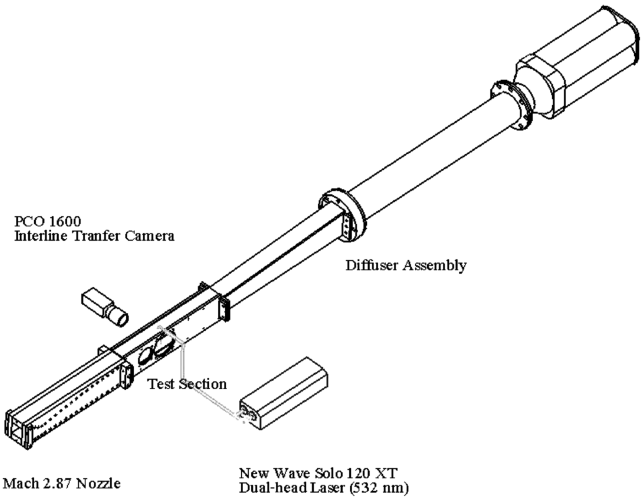

Fig. 1 Schematic of the supersonic wind tunnel.

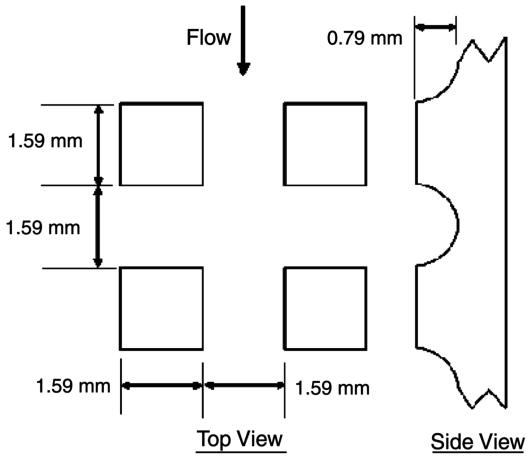

a) Schematic

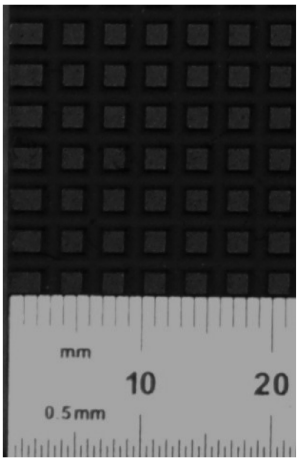

b) Photograph

Fig. 2 Square roughness topology.

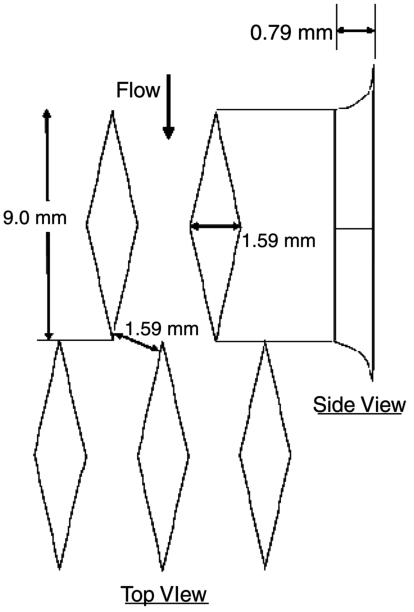

a) Schematic

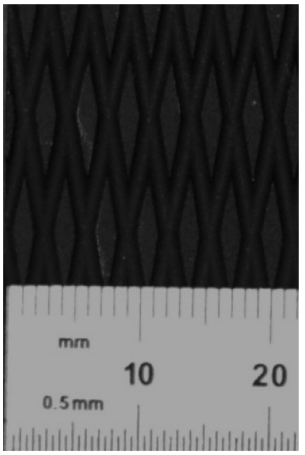

b) Photographs

Fig. 3 Roughness topology.

axial direction at the freestream conditions before reaching the test-section entrance. The boundary-layer thickness at the nozzle exit, based on pitot surveys, was 10.0 mm.

B. Model Design

Two roughness topologies were designed to produce fundamentally different near-wall distortions. Schematics and photographs of the roughness patters are given in Figs. 2 and 3 for the square and diamond models, respectively. Measurements on an aerodynamically smooth wall at the same flow conditions were accomplished for comparison purposes. The smooth-wall model was manufactured from polished Plexiglas. The surface polish was Mothers brand 05100 mag and aluminum polish. The estimated roughness Reynolds number k^+ was 0.14. The wind-tunnel model characteristics are summarized in Table 1, and a brief description of roughness topologies is presented next.

The first roughness topology was designed to produce the canonical "sand-grain" behavior seen in low-speed flow. More specifically, Latin and Bowersox [15,24] demonstrated that a 3-D machined square topology followed the accepted correlations. To further foster the accepted scaling, the roughness-element spacing was selected to produce the "d-type" roughness characteristic; that is, $\lambda/w = 2.0$. Perry et al. [3] remarked that for d-type periodic roughness elements, "stable vortices are set up in the grooves and eddy shedding from the elements into the flow will be negligible." Thus, strong localized shock waves were not expected for this roughness topology. A schematic of the element shape is given in Fig. 2a, and the expected recirculation flow structure is illustrated in Fig. 4a. The model was machined from Plexiglas. The roughness elements were produced by machining 0.79-mm-deep channels using a 1.59-mm-diam (1/16-in.-diam) ball end mill. The resulting roughness elements had a length and width of 1.59 mm and were separated from adjacent elements by the 1.59-mm-wide channel. A photograph of the roughness element is given in Fig. 2b, in which the models were painted black to improve the quality of the photograph.

The second roughness topology was designed to produce significant localized shock- and expansion-induced flow distortions. To accomplish this goal, diamond roughness elements were designed to have attached leading oblique shock waves, followed by a Prandtl–Meyer expansion. A schematic of the element shape is given in Fig. 3a, and the expected flow structure is illustrated in Fig. 4b. The major axis of the roughness element was aligned with the flow direction, and the leading edge had a 10.0-deg half-angle. As indicated by Liepmann and Goddard [13], the skin friction at the surface is related to the drag of the surface. Thus, the size of the elements was selected so that the frontal blockage area closely matched the square elements, and the main difference in the surface

Table 1 Surface conditions

Model	k, mm	a, mm	b, mm	w, mm
Smooth plate	0.0	0.0	0.0	0.0
Square roughness	0.8	1.6	1.6	1.6
Diamond roughness	0.8	1.6	9.0	1.6

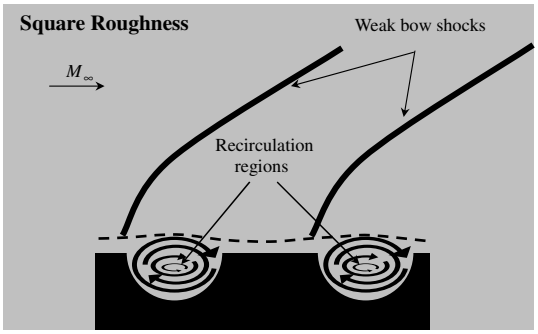

a) Side view of square roughness

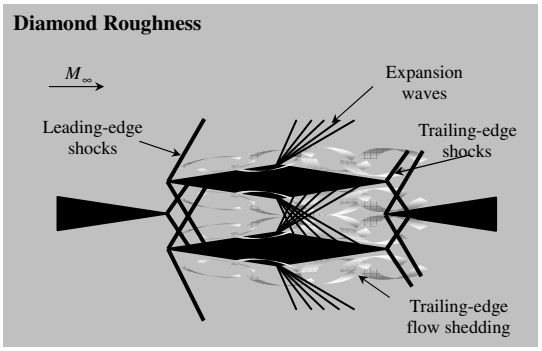

b) Top view of diamond roughness

Fig. 4 Simplified sketches of roughness-element near-wall flow patterns.

skin friction was the drag coefficient on the elements. This led to diamond elements that were 9.00 mm long, 1.59 mm wide, and 0.79 mm tall. The pattern was machined into Plexiglas, as described in the previous paragraph. Based on the near-wall measurements of Mach number made by Latin and Bowersox [24], it was expected that the roughness elements would protrude into the supersonic portion of the boundary layer. Even though the ratio between the roughness period and cavity width matched that of the square roughness elements, it was expected that the swept nature of the groove would allow the vortex structures to flow around elements and be shed into the flow at the trailing edge, as illustrated in Fig. 4b.

C. Coordinate System, Reference Conditions, and Measurement Locations

The coordinate system for the present study was defined such that x was in the streamwise direction, y was vertically up measured from the tunnel floor, and z completed the right-hand system. The origin of the coordinate system was on the tunnel floor at the center of the nozzle exit. The reference velocity U_{ref} was defined as the nozzle exit velocity (625 m/s). The nozzle exit boundary-layer thickness (10.0 mm) was defined as the reference length δ_{ref}. Data were acquired at three locations centered on $x/\delta_{\text{ref}} = 15.9, 29.8$, and 41.3. The roughness-element plates initiated at $x = 0$. The leading edge of the 18th row of diamond elements was at $x/\delta_{\text{ref}} = 15.5$. This location corresponded to the 49th row of square roughness elements. The first location is the primary measurement plane reported in this paper.

D. Schlieren Photography

A Z-type two-mirror schlieren system was used. The knife edge was aligned for density gradients normal to the wall. The schlieren image was recorded by a Nikon D50 SLR camera.

E. Pressure-Sensitive Paint

Surface pressure distributions were documented using pressure-sensitive paint (PSP) [25]. The paint used in the present tests was a UNC405 produced by Innovative Scientific Solutions, Inc., (ISSI). The binary paint was designed for a pressure range of 10–150 kPa, which covered the surface pressures in this study. Six coats, each approximately 10 μm thick, were sprayed onto each test-section model. The models were cured with a heat gun for approximately 15 min after the final coat was applied. An ISSI, Inc. LM-series LED array light source was used to excite the PSP and a PCO 1600 camera was used to image the luminescence over a 5.08 by 3.81 cm area. The 1600 by 1200 camera resolution was reduced to 800 by 600 via pixel binning for enhanced signal-to-noise ratio.

The software used to process the images was ISSI's OMS Lite version 1.1. The software was capable of resolving errors due to photo-detector noise, nonuniform image illumination, and model deformation using a two-dimensional displacement evaluation that included image registering. For each run, four images were acquired: a background image with all light turned off, an initial wind-off image taken just before the tunnel was started, and with the LED array on, a wind-on image with the tunnel running long enough to reach thermal equilibrium and a final wind-off image taken immediately after the tunnel was stopped. Before the tunnel runs, eight marker dots were applied to the surface with a felt-tip pen at known locations to account for model distortions. The location of the marker dots was manually entered into the OMS software, and image registration was accounted for using an eight-step quantum pixel energy distribution [26] algorithm with three iterations and an initial box size of 16 by 16 pixels. Because of the paint's thermal and pressure dependence, the PSP was calibrated by a second-order least-squares approximation with known temperatures and pressures. Finally, a four-pixel box-smoothing filter was applied to sharpen the linear interpolation of PSP values. Comparisons were made with the smooth model, and the PSP values were within 1.0% of the pressure tap data. However, due to the small size of the roughness elements, it was not possible to resolve the pressure on the surface of the elements or within the channels using static pressure ports. The measurement uncertainty analyses for the PSP, as well as the remaining diagnostic methods, are summarized in Sec. II.H.

F. Pitot Pressure

The pitot pressure was measured with an Omega brand PX303 pressure transducer (with a range of 0–690 kPa and $\pm 0.25\%$ full-scale accuracy). The pressure probe had a 1.6-mm-diam tube with an inner diameter of 0.8 mm. The end of the tube was crimped so that the entrance height was 0.2 mm. The probe was traversed in the wall-normal direction by a Velmex model MA2508P40 linear translation stage that contained a turn screw that had 15.75 turns per centimeter. The translation stage was moved by a Vexta PK2608-02A 400-step stepper motor. The stepper motor was operated by an S100 three-channel stepper-motor controller that was controlled by a PC running the S100 SMC software. The probe was translated at 1.9 cm/min. The position of the probe was monitored with a P3 America, Inc. ISDG linear variable displacement transducer (0.5% full scale) with a stroke length of 20 mm. The probe pressures were sampled at a rate of 1.0 kHz, and each data point was the result of a 100-point average.

G. Particle Image Velocimetry

Particle image velocimetry [27] was used to measure velocity fields across the boundary layer with sufficient spatial resolution to resolve the flow over the roughness elements. For the present tests, the tunnel was seeded by a TSI six-jet atomizer (model 930628) with Bertolli extra-light olive oil. The documented mean particle diameter was 0.6 μm, and the 3-dB frequency response of the particles was documented at 60–200 kHz [28]. The tracer particles were illuminated using a dual-port/dual-head New-Wave Solo 120XT PIV laser. Each laser head had a maximum energy output of 120 mJ at 532 nm. The pulse width was 4 ns and had a maximum frequency of 15 Hz. The beam out of port 2 was cross-polarized using a crystal quartz half-wave plate. In front of the first laser port there was a high-energy polarizing cube beam-splitter that provided efficient narrowband polarization. The laser beams were then guided to the test section using 90-deg bending prisms constructed of BK7 glass with AR coatings. A BK7 focus lens with a focal length of 500 mm was used to focus the beam so that the waist was located just above

the test-section floor. A nominally 1.5-cm-wide and 1.0-mm-thick laser sheet was formed using a BK7 plano-concave cylindrical lens. The laser sheet was located along the centerline of the wind tunnel. The camera used was a Cooke Corp. PCO 1600 interline-transfer CCD camera with a Nikon 60-mm lens. The camera trigger, laser Q-switch, and laser flashlamp were all controlled by a Quantum Composers model 9618 pulse generator. The camera frame-grabbing software was Camware version 2.13.

The PIV images were reduced to velocity fields with the ISSI brand dPIV 32-bit analysis code [29]. For the present measurements, a three-step adaptive cross correlation was used, with successive interrogation sizes of 128×64, 64×32, and 32×16 pixels and a 50% overlap. To enhance the intensity of correlation peaks relative to random noise, a four-map correlation-multiplication process filter was used. A consistency postprocessing filter was used to improve the adaptive correlation calculation. First- and second-order turbulent statistics were created using an in-house code that ensemble-averaged the velocity vector fields. For the present study, 5000 image pair samples were acquired at each measurement location. The measurement grid consisted of 71 by 34 data points, for which the axial and transverse separations were 0.35 and 0.71 mm, respectively. This resolution was sufficient to compute gradients in the mean and turbulent flow across the roughness elements.

H. Measurement Uncertainties

The measurement uncertainties for the present study are summarized in Table 2. The experimental uncertainties were accumulated with a Euclidean norm [30]. The uncertainties in the freestream stagnation conditions included transducer-measured repeatability. The reported uncertainty for the PSP used in the pressure experiments was 300 Pa, which translated into $\sim$1.5% of the freestream pressure. However, in the present tests, the measured uncertainty was approximately 11.0%. The reasons for the discrepancies are believed to be due to nonuniformities in the application, lighting, and curing (heated) of the paint. The measured variance in the pitot probe data agreed with the reported transducer uncertainty. The axial position was taken as half the smallest division on the calibration scale, and the transverse probe position uncertainty was taken as approximately half the tip height. The boundary-layer thickness uncertainty accounted for the uncertainties in position and velocity, for which the sensitivity to the velocity uncertainty was estimated with a 1/7th power law. The uncertainty analysis of the PIV data accounted for correlation mapping error and the conversion error from the physical length scale to the appropriate number of camera pixels. The axial position uncertainty was the same as that of the pitot probe. The transverse position uncertainty was taken as that of the wall position, which was known to within two pixels on the camera array, which corresponded to $\sim$0.1 mm. The estimated uncertainty in the statistical quantities was determined using a 95% confidence interval [30]. The variance was determined assuming a normal distribution and a total of 5000 instantaneous velocity vector fields. The uncertainty in the transverse velocity was taken to be the magnitude of the axial velocity uncertainty. Inner-variable scaling was facilitated by estimating the wall shear stress from PIV turbulent-shear-stress data in the near-wall region via the Couette flow approximation. The wall shear stress uncertainty was then taken as that of the turbulent shear stress. The uncertainty in the velocity gradients was a combination of the uncertainties in the positions, the mean velocity measurements, and the associated finite difference scheme.

I. Flowfield Three-Dimensionality

In the present investigation, data were acquired along the centerline of the tunnel. For the smooth and square roughness patterns, it was reasonable to assume that the flow statistics were nominally two-dimensional for the present cases in which $\delta/k \sim 15$, as indicated by Reynolds et al. [31]. However, the diamond roughness topology was designed to produce significant secondary flow. To estimate the effects of this three-dimensionality on the flow, additional PIV measurements were taken across the span. The first measurement was taken along the center of the lateral span of a roughness element, and a second measurement was shifted 0.4 mm in the z direction to the midpoint between the element center and element edge. The transverse velocity component, plotted in Fig. 5, showed that small systematic differences in the velocity were resolved. The dark vertical structure located near $x/\delta_{\text{ref}} = 15.75$ and the bright axial structure near $y/\delta_{\text{ref}} = 0.15$ were the result of laser reflections. Away from these reflections (the data in Fig. 5), the maximum difference was nominally 3.0 m/s. This velocity difference corresponded to 0.4% of the local axial velocity, which was close to the 0.5% measurement uncertainty listed in Table 2. The axial velocity had a similar difference. The reflections in Fig. 5 demonstrate a key challenge associated with the present study. Thus, for the present work, the small three-dimensional effects were neglected and the laser sheets were arbitrarily positioned in the spanwise direction to minimize laser reflections.

Table 2 Uncertainties

Variable	Error
P_{01}	3.0%
T_{01}	3.0%
PSP	11%
x, y, mm	0.4, 0.1[a]
P_{02}/P_{01}	0.4%
δ	6.0%, 5.0%[b]
U	0.6%, 0.5%[b]
U^+_{eff}	6.1%, 6.0%[b]
$\overline{u'u'}$, $\overline{v'v'}$	4.0%
$\overline{u'v'}$	8.0%
dU/dx, dV/dx, dV/dy, dU/dy	3.0%
$P_{xx}/\bar{\rho}$, $P_{yy}/\bar{\rho}$, $P_{xy}/\bar{\rho}$	23.0%

[a]Applies to both pitot probe and PIV
[b]Left entry: pitot probe, right entry: PIV

III. Results and Discussion

A. Schlieren Photographs

The schlieren photographs given in Fig. 6 were acquired at the second test location. The lack of optical access prevented measurements at the first and third locations. The flow direction was from left to right and the surface roughness was located along the lower surface. The dark band at the floor and the light band at the ceiling represent the lower- and upper-surface boundary layers, respectively. A wave that formed at the intersection of nozzle exit and test section was observed. These intersection waves were weak, and the disturbances were undetectable in the quantitative measurements. The square-roughness-element schlieren image illustrates weak detached waves, which formed at the leading edge of the roughness elements, permeated the boundary layer, and extended into the freestream. Relative to the square model, the diamond-roughness-model schlieren images displayed a strong pattern of

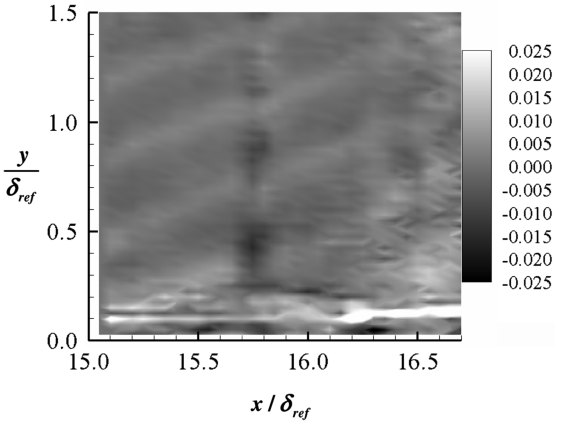

Fig. 5 Diamond-roughness-element velocity difference $\Delta V/U_{\text{ref}}$.

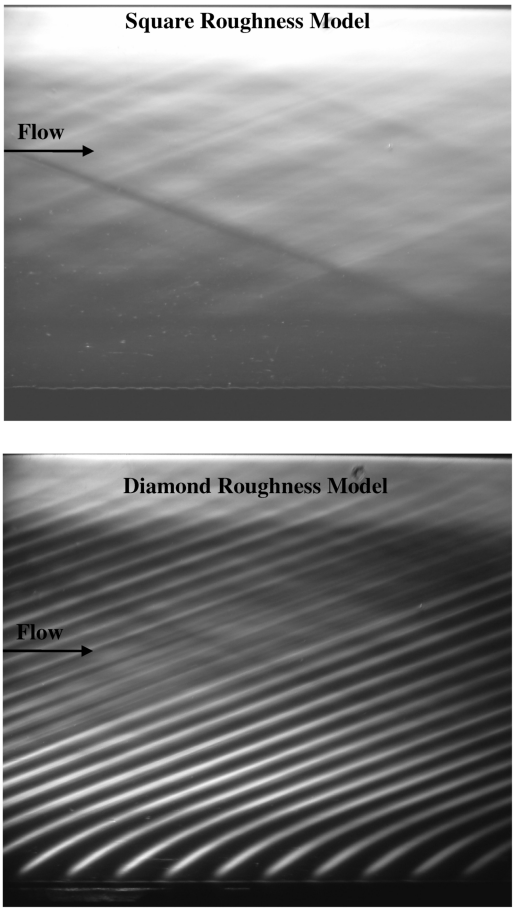

Fig. 6 Schlieren photograph at the second test location for the roughness models (roughness elements were on the lower surface).

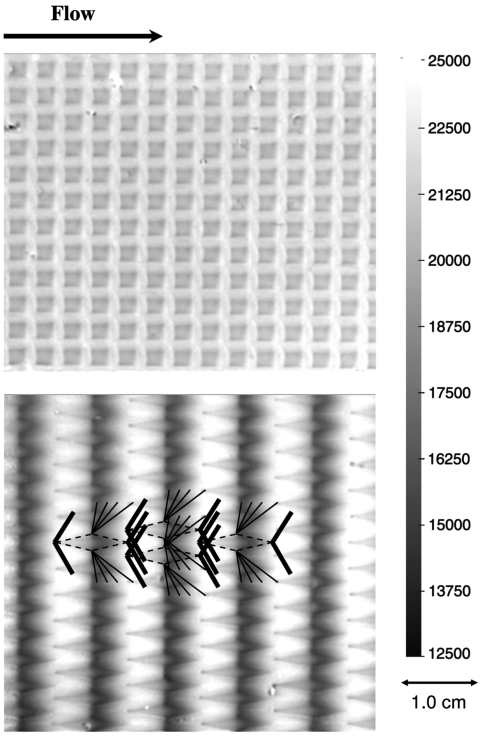

Fig. 7 Surface pressure distributions for square roughness (top) and diamond roughness (bottom) models at the second test location; flow is from left to right and the units on the scale are in pascal.

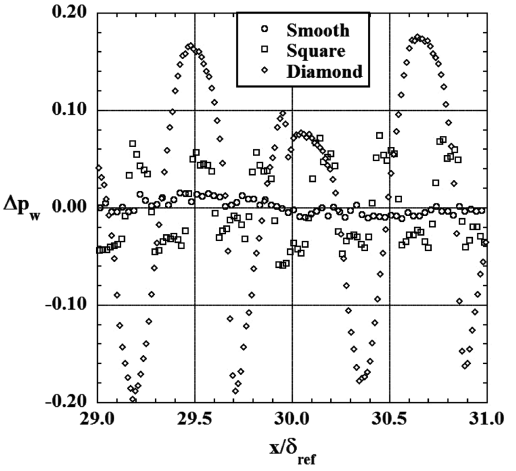

Fig. 8 Axial surface pressure profiles.

waves originating from the lower surface at the leading edge of the roughness elements. The waves traversed into the tunnel freestream. The strong wave pattern masked the floor boundary layer and the nozzle intersection wave.

B. Pressure-Sensitive Paint

The surface pressure distributions were obtained with PSP. The results for the two rough-wall models at the second test location are displayed in Fig. 7. For a comparison of the change in mean pressure across the roughness elements, an axial profile of the Δp_w, the variation of the local surface pressure from the mean, is plotted in Fig. 8. The surface pressure distributions for the smooth-wall model were uniform to within the measurement uncertainty. For the square roughness model, the PSP contour and axial plot showed a relatively modest oscillating pressure distribution, in which the pressure in the channel was about 10% larger than that over the roughness-element surface. This observation indicated the presence of the weak detached waves. When coupled to the schlieren photographs, the PSP results confirmed the expected flow structure described in Sec. II.B for the square roughness.

The diamond-roughness-model PSP image in Fig. 7 revealed a three-dimensional pressure field, with strong alternating axial bands of adverse and favorable pressure gradients. For clarity, a sketch of the expected local shock and expansion structure was superimposed on the PSP images of the diamond roughness model (Fig. 7). On the front half of the roughness element, there was an increase in the pressure due to the oblique shock waves. The pressure then decreased as a result of the expansions. The high- and low-pressure regions of the individual elements overlapped adjacent elements, producing pressure gradients that exhibited periodic axial variation (± 10 to 18% of the mean wall pressure). The amplitude of the pressure rise was found to depend on the position relative to the roughness elements. The two larger peaks at $x/\delta_{\text{ref}} = 29.5$ and 30.7 correspond to the regions between the leading edges of two adjacent elements, and the two smaller ones correspond to the pressure directly on the roughness elements; this is shown schematically in Fig. 7. The variation in the pressure peaks demonstrated that the flow had the expected strong axial periodic variations.

C. Mean Boundary-Layer Profiles

Mean pitot pressure, velocity, Mach number, and velocity gradient data were obtained from the pitot probe and PIV instruments at $x/\delta_{\text{ref}} = 15.9$, 29.8, and 41.3 cm downstream of the nozzle exit. The pitot pressures were normalized by upstream stagnation pressure, and the traverse distance was normalized by the local boundary-layer height. Profiles of p_{0_2}/p_{0_1} for the smooth and square roughness models are presented in the upper plot in Fig. 9. The three profiles for the smooth wall nearly collapsed. A similar collapse was observed for the square roughness, for which as expected [24], the profiles were less full than those for the smooth plate. These data imply

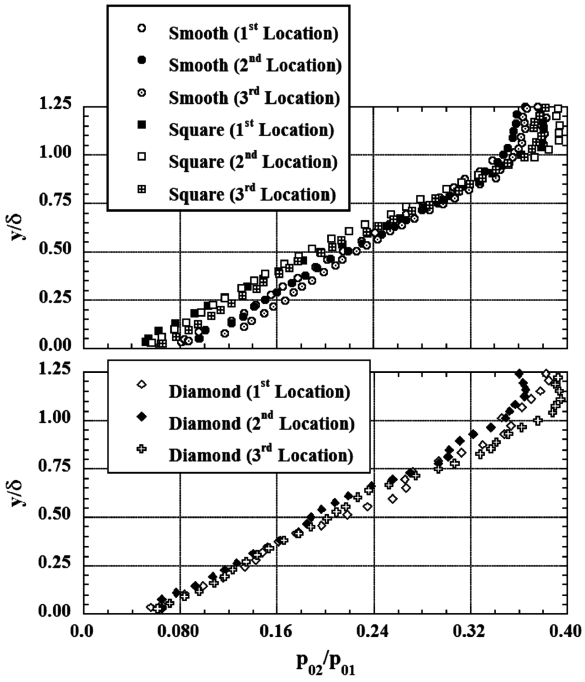

Fig. 9 Stagnation pressure profiles.

equilibrium boundary layers, for which the pressure gradient parameter ($\delta^*/\tau_w \cdot \mathrm{d}p/\mathrm{d}x$) due to boundary-layer growth was estimated at approximately 0.04. The sonic points were defined as the height above the wall below which the flow was subsonic. These points were found to be the inner logarithmic region of the boundary layer (shown in a later figure). The locations correspond to $y/\delta = 0.05$ and 0.07 for the smooth and square roughness models, respectively. Finally, in the near-wall region, the pitot probe size was comparable with the height above the floor. However, corrections were not applied to the pitot data, because they were used primarily to verify the accuracy of the PIV data for y/δ greater than approximately 0.2.

The pitot profiles for the diamond roughness had zigzag patterns, which resulted from the probe traversing across shocks and expansions generated by the roughness elements and are thus presented separately in the lower plot of Fig. 9. The magnitude of the periodic variations was observed to diminish at the downstream measurement locations. This trend was expected, because as the boundary layers became thicker, the sonic line rose and the portion of the roughness elements that protruded into supersonic flow was reduced, thereby reducing the strength of the shocks. The apparent overshoot near the edge of the boundary layer for the diamond-model pitot traces was the result of the waves (see Fig. 6) that traversed the boundary layer and extended into the freestream.

Velocity contours were produced from PIV data at all test locations. Representative contours from the first test location are given in Fig. 10. The velocity components were normalized by the reference velocity. The smooth- (Fig. 10a) and square-roughness-model (Fig. 10b) axial velocity contours were uniform in the x direction and decreased in the transverse direction in the expected manner. The corresponding $\bar{v}$ components were very small (not shown here). On the other hand, the $\bar{u}$-component contour plot for the diamond roughness model (Fig. 10c) exhibited a wavy pattern throughout the boundary layer and into the freestream. A series of alternating negative and positive bands of $\bar{v}$ were observed (Fig. 10d), in which the values varied between $\pm 3\%$ of the freestream velocity. The patterns in the velocity field corresponded to the shock and expansion waves shown in the schlieren photographs in Fig. 6, in which, for example, as mentioned in Sec. II.C, the leading edge of the 18th row of diamond elements was near $x/\delta_{\mathrm{ref}} = 15.5$.

Velocity profiles were extracted from the PIV data and computed from the pitot data by using the Rayleigh–Pitot formula above the sonic point and the isentropic relations below the sonic point to compute the local Mach number. The velocity was then estimated assuming a constant total temperature across the boundary layer. Law-of-the-wall and defect-law plots were then produced from both the PIV and pitot pressure data. The wall shear stress was estimated from the PIV turbulent-shear-stress measurements assuming Townsend scaling [32]. The turbulent shear stresses with Townsend scaling are given in Fig. 11. For the present measurements, the planar

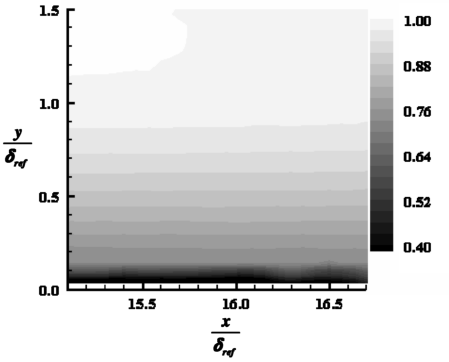

a) U/U_{ref} for the smooth model

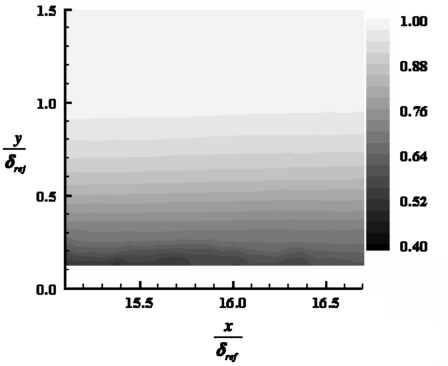

b) U/U_{ref} for the square roughness model

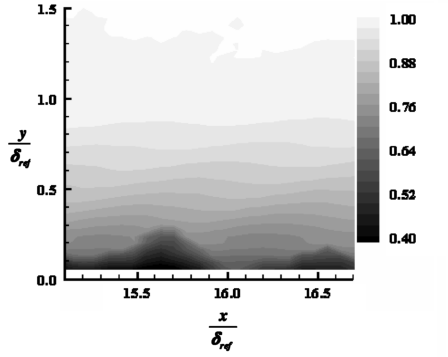

c) U/U_{ref} for the diamond roughness model

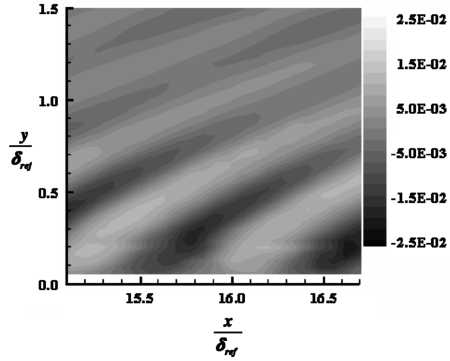

d) V/U_{ref} for the diamond roughness model

Fig. 10 Velocity contours at $x/\delta_{\mathrm{ref}} = 15.9$.

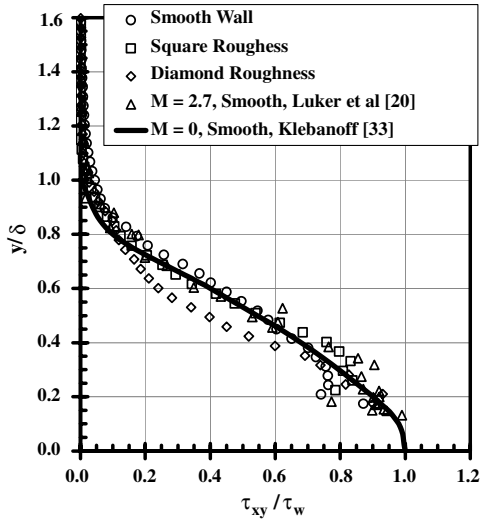

Fig. 11 Turbulent-shear-stress distributions at station 1.

PIV data were averaged in the axial direction over a range of $\sim 1.6\delta_{\text{ref}}$ to minimize the effects of the local roughness topology. Also shown in Fig. 11, for comparison purposes, are the incompressible data of Klebanoff [33] and the supersonic data of Luker et al. [20]. The overall shapes of the present smooth and square roughness profiles followed the Klebanoff [33] trend, as did the smooth-wall data of Luker et al. [20]. However, the diamond stresses were 30% below the trend on the outer region of the boundary layer. This was the result of the influence of the diamond element shocks and expansions on the turbulent shear stresses; this is subsequently described in more detail. The equivalent sand-grain heights were computed with the method described in Antonia and Wood [7]. The resulting boundary-layer properties at $x/\delta_{\text{ref}} = 15.0$ are summarized in Table 3.

Velocity profile data were extracted from the PIV data at $x/\delta_{\text{ref}} = 15.0$. Inner and outer scaled plots with van Driest II compressibility scaling [34] are displayed in Figs. 12a and 12b respectively. The diamond roughness data were not included in Fig. 12 because of the periodic flow variations. The smooth-model PIV and pitot data exhibited good agreement with each other and the accepted law-of-the-wall correlation (Fig. 11), given by

$$\bar{u}^{+}_{\text{eff}} = \begin{cases} y^{+}, & y^{+} < 10 \\ \frac{1}{\kappa}\ell_n(y^{+}) + B + \frac{2\Pi}{\kappa}\sin^2\left(\frac{\pi}{2}\frac{y}{\delta}\right), & y^{+} \geq 10 \end{cases} \tag{1}$$

where the constants κ, B, and Π [35,36] were set to 0.4, 5.5, and 0.8, respectively. The square roughness model produced the expected downward shift of the law of the wall for both PIV and pitot data, again showing very good agreement with each other. The downward shift was $\Delta\bar{u}^{+}_{\text{eff}} \approx 12.2$.

The smooth and square roughness PIV and pitot velocity data collapsed onto the incompressible defect-law theory when van Driest II scaling was used. The resulting plots are shown in Fig. 12. The accepted correlation for the defect law is given by

$$\frac{\bar{u}_{\text{eff}} - \bar{u}_{\text{eff},e}}{u^*} = \frac{1}{\kappa}\ell_n\left(\frac{y}{\delta}\right) - \frac{2\Pi}{\kappa}\left[1 - \sin^2\left(\frac{\pi}{2}\frac{y}{\delta}\right)\right] \tag{2}$$

These data imply that the accepted theory provides a good prediction of the average wall behavior for smooth walls and rough walls, for which the surface roughness produces minimal local flow distortions. The diamond roughness plots were significantly more complicated because of large variations in the measured turbulent stresses (used here to estimate the wall shear stress) and the velocity profiles.

Table 3 Boundary-layer properties at $x = 15.9$ cm

Model	δ, mm	C_f	k_s/k	k_s^{+a}	u^{*a}, m/s
Smooth	11.0	0.0013	0.00	0	23.3
Square	11.6	0.0026	0.73	310	35.2
Diamond	$\sim$11.0	0.0014	0.07	23	25.9

[a]Based on freestream conditions listed in Sec. II.A

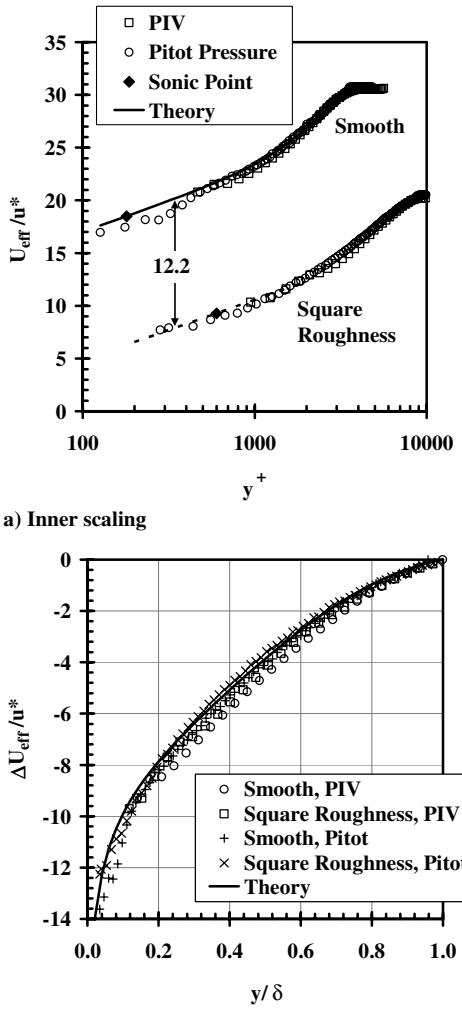

Fig. 12 Velocity profiles at station 1.

Strain-rate contours were created from the PIV velocity field data using a second-order explicit-forward finite difference scheme. The primary velocity gradient was found to be dominant for all three models. The extra-strain rates for the smooth-wall model were all very small. For the square-roughness-element models, the extra-strain rates were essentially negligible in the outer 70% of the boundary layer. However, in the lower 30%, small periodic variations, which corresponded to the width of the roughness elements, were observed. The diamond roughness extra-strain rates (Fig. 13) exhibited a wave pattern across the boundary layer. Although the extra-strain rates were not as strong as the primary gradient, their presence indicated additional turbulence-production mechanisms.

Axial profiles of the strain rates for the diamond roughness model are plotted in Fig. 14 at $y/\delta = 0.3$. In this plot, each strain rate was normalized by the summation of all strain rates ζ, which had a constant value in the axial direction of approximately $0.53 \cdot (\delta_{\text{ref}}/U_{\text{ref}})$. As expected, the dominant strain rate at all locations was the principle strain rate. For the diamond-element case, the principle strain rate varied over a range of $\pm 30\%$ of the total strain rate value, depending upon the proximity to the leading edge of a roughness element. The $\mathrm{d}U/\mathrm{d}x$ and $\mathrm{d}V/\mathrm{d}x$ strain rates had nearly equal and opposite values at all locations, with the values peaking at $\pm 25\%$ of the total strain. Similarly, the change in the principle strain rate $\mathrm{d}U/\mathrm{d}y$ was offset by $\mathrm{d}V/\mathrm{d}x$ and any contributions from the

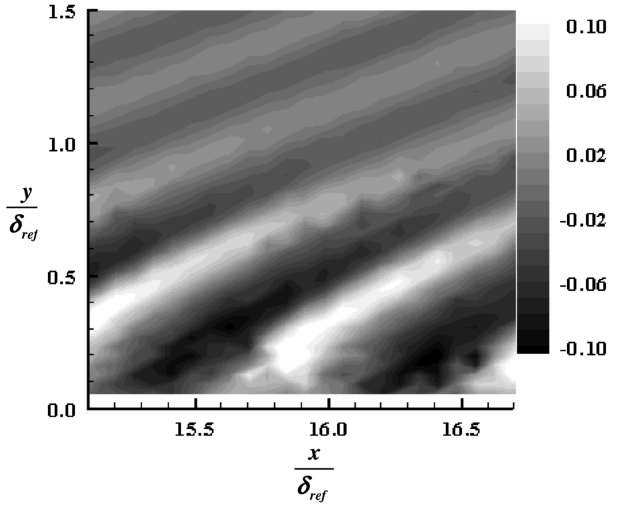

Fig. 13 Contour of the dV/dx extra-strain rate normalized by $\delta_{\text{ref}}/U_{\text{ref}}$ for the diamond roughness model.

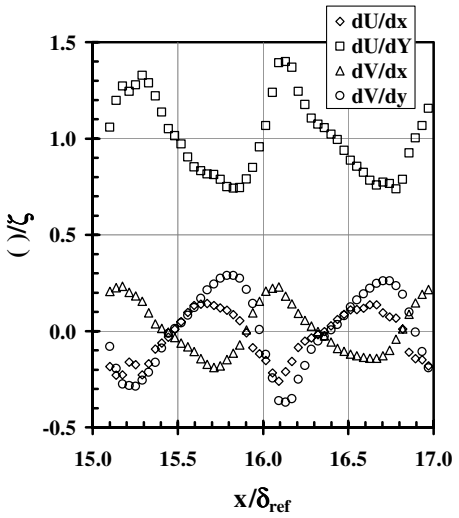

Fig. 14 Axial profiles of the strain rates at $y/\delta = 0.3$.

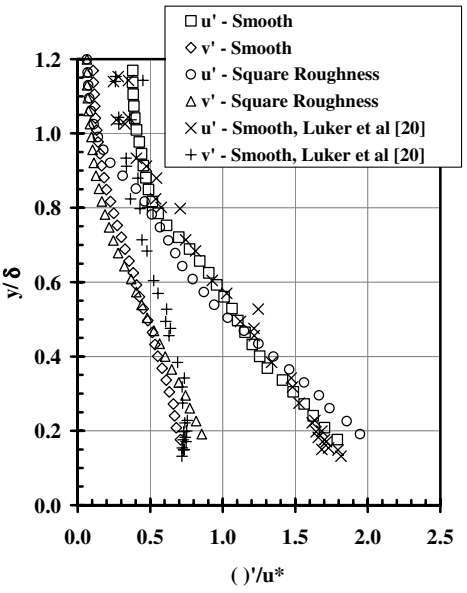

Fig. 15 Turbulence-intensity profiles for the smooth-wall and square roughness models at station 1.

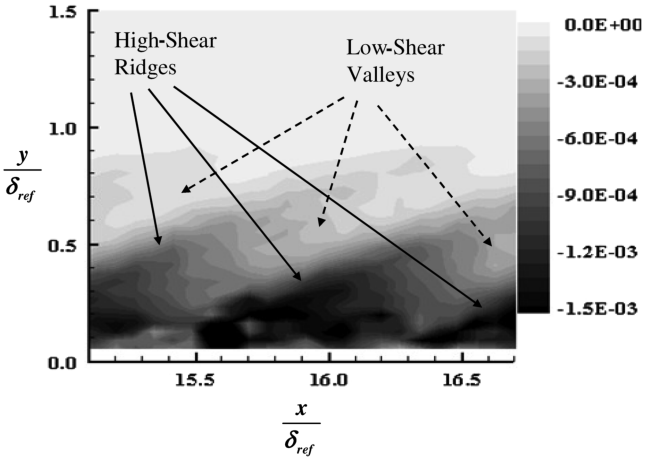

Fig. 16 Diamond-roughness-model turbulent-shear-stress contour.

spanwise velocity gradients. The smooth- and square-roughness-model strain rate behaviors followed the expected trend, in which the principle axis was two orders of magnitude larger than any of the other extra-strain rates. The measured values of the maximum distortions across the boundary layers are listed in Table 4. The distortions across the diamond elements were considered strong, and as will be seen later, the turbulence was very responsive to these distortions. The distortions for the square element model were comparatively weak. However, near the wall, the square roughness distortions may have been larger than was resolvable in the present experiment.

D. Turbulence Results

Axial and transverse turbulence-intensity profiles were plotted for the smooth and square-roughness-element models, because the axial flow variations were minimal. The profiles are shown in Fig. 15, in which the data were averaged in the axial direction, as was done for the mean velocity profiles. The corresponding Reynolds shear stress data are shown in Fig. 11. To facilitate comparison with previous studies, the turbulence-intensity data in Fig. 15 were normalized by the friction velocities listed in Table 3. The smooth-wall data of Luker et al. [20] are in included for comparison purposes, because the flow conditions were similar to the present study. The present smooth-wall data for the turbulence intensities (Fig. 15) and Reynolds shear stresses (Fig. 11) were in good agreement with the Luker et al. data. The square-roughness-model results appeared to collapse onto the smooth-wall trends with the scaling used in Figs. 11 and 15. This finding agrees with the low-speed study of George and Simpson [6].

A contour plot of the turbulent shear stress for the diamond roughness model is presented in Fig. 16. The turbulence stresses were normalized by the square of the reference velocity. This contour showed an alternating pattern of low and high shear stress across the boundary layer that was closely aligned with the waves observed in the schlieren photographs. For example, a high-stress region was observed to begin at the floor near $x/\delta_{\text{ref}} = 15.5$, which, as mentioned in Sec. II.C, corresponded to the leading edge of the 18th row of diamond elements. The high-stress region moved up and to the right along the wave. Just downstream of the high-stress region was a region of low stress, which corresponded to the expansion

Table 4 Measured distortion parameters

Model	$d_{\max}$
Smooth wall	0.00
Square roughness	−0.01
Diamond roughness	−0.3 to 0.4

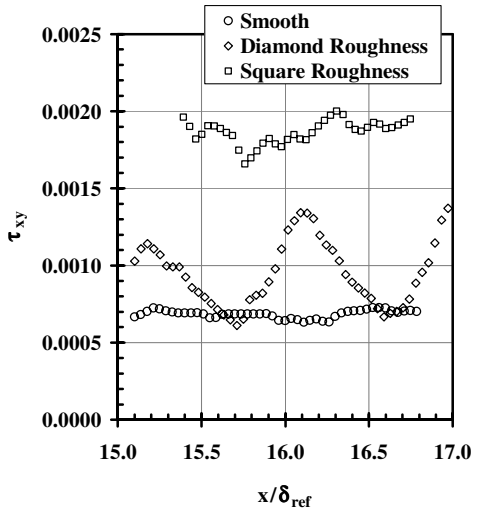

Fig. 17 Axial profiles of Reynolds shear stress $/\bar{\rho}U_{\text{ref}}^2$ at $y/\delta = 0.3$.

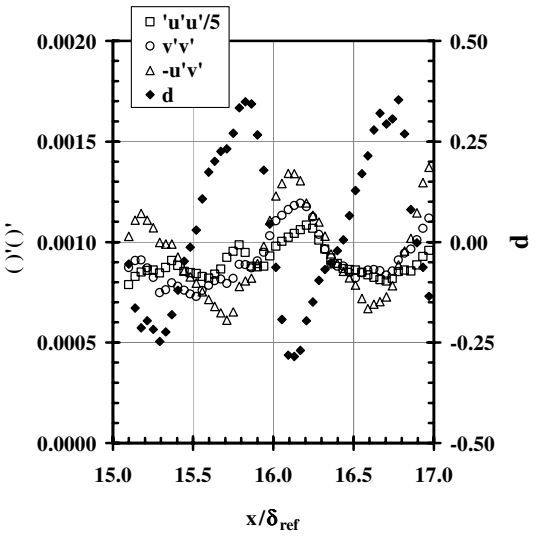

Fig. 18 Reynolds stresses $/\bar{\rho}U_{\text{ref}}^2$ and the distortion of the diamond roughness model at $y/\delta = 0.3$.

region on the diamond element, shown schematically in Fig. 7. This pattern repeated in both the upstream and downstream directions, and the period corresponded to approximately the diamond-roughness-element length. The high-shear-stress ridges and low-shear valleys are annotated in Fig. 16 for clarity. The turbulence-intensity contours showed similar patterns.

To better quantify the variations of the turbulence, axial plots were extracted at $y/\delta_{\text{ref}} = 0.3$. First, the Reynolds stresses for the three models are compared in Fig. 17. The Reynolds stress for the square roughness model was nominally 150% greater (i.e., a factor of 2.5) than the smooth-wall values at this location within the boundary layer. The small axial variations (compared with the diamond plate) correspond to the weak waves produced by roughness topology. Conversely, the diamond-roughness Reynolds stress varied periodically by nearly a factor of 2. The average increase in the Reynolds shear stress at this location within the boundary layer was about 40% higher than the smooth wall, which was a significant reduction compared with the square roughness. Although the magnitudes of the periodic variations changed, the trends continued across the boundary-layer height. The diamond-roughness-model axial and transverse stresses were compared with the Reynolds shear stresses, as shown in Fig. 18. This comparison indicated that the axial and transverse turbulence-level maximums and minimums correspond to the Reynolds shear stress maximum and minimums. Thus, it was expected that the extra-strain rates [16] and the associated production were the main cause for the observed variations. To illustrate the connection between the turbulent shear stresses and the velocity gradients for the diamond plate, axial profiles of the Reynolds stress and the mean flow distortion (which, as described in Sec. III.C, was proportional to the dV/dy extra-strain rate) are included in Fig. 18. The close phase between turbulence minima with distortion maxima, and vice-versa, implied that turbulence levels were strongly influenced by the extra production.

E. Turbulent-Stress Production

The axial P_{xx}, transverse P_{yy}, and shear stress P_{xy} production were computed from the PIV measurements. Representative axial profiles of the turbulent-stress production for all three components are plotted in Fig. 19 for $y/\delta_{\text{ref}} = 0.3$. For the smooth-wall models, the dominant production terms were the axial production term P_{xx} and the turbulent-shear-stress production term P_{xy}. The transverse turbulent-stress term P_{yy} was an order of magnitude lower than the other two. This was primarily due to the absence of the primary velocity gradient from P_{yy}. Similarly, the dominant production terms for the square roughness model were P_{xx} and P_{xy}. At $y/\delta_{\text{ref}} = 0.3$, the P_{xx} and P_{xy} terms were 200 and 400% greater, respectively, than the smooth-wall values. At this y location, the square roughness production plots showed evidence of a periodic pattern, in which the

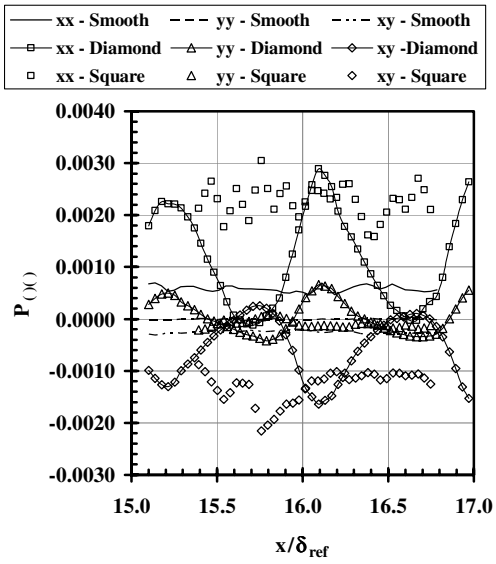

Fig. 19 Axial profiles of turbulent-stress production $(\cdot\delta_{\text{ref}}/\bar{\rho}U_{\text{ref}}^3)$ at $y/\delta = 0.3$.

period was similar to the roughness-elements wavelength. Thus, it was inferred that although the near-wall pressure waves due to the roughness elements may have been small, the production was significantly amplified and the effect of the topology was present in the traces.

For the diamond roughness, the relatively strong oblique alternating velocity gradients, noted in previous sections, created the alternating production fields shown in Fig. 19. These production fields generated and subsequently destroyed the turbulent stresses. The production components that contained the primary velocity gradient remained dominant, but the extra-strain rates were also significant. At the minimum, the P_{xx} term was zero, whereas the P_{xy} term became a sink term for Reynolds stress. The maxima values for P_{xx} and P_{xy} were 300 and 400% greater than the smooth-wall values, respectively, which was much larger than the square roughness model. On the average, diamond roughness models P_{xx} and P_{xy} were approximately midway between those for the smooth and square roughness models. The maxima and minima values for P_{xx}, P_{yy}, and P_{xy} corresponded with each other. It is noted that each of the components of the P_{yy} production term contributed in a complementary manner to the amplification and deamplification of the turbulent shear stress. Additionally, the transverse turbulent-

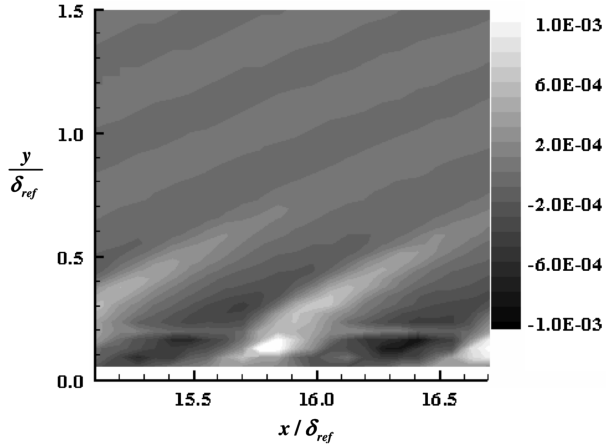

Fig. 20 Diamond roughness turbulent-stress production contours.

stress production term P_{yy} was significant, with levels varying between positive and negative values. The P_{yy} maxima and minima values were similar in magnitude to the P_{xx} production term for the smooth-wall model. Finally, an example production contour for the diamond roughness model is given in Fig. 20. The P_{yy} production was plotted because the absence of the principle strain rate allowed a clearer view of the extra production near the wall, which was not the case for P_{xx} and P_{xy}. The horizontal line located near $y/\delta_{\text{ref}} = 0.2$ resulted from a laser sheet reflection. The production contour in Fig. 20 demonstrated how the waves and associated strain rates established by the roughness elements altered the turbulence production across the boundary layer.

IV. Conclusions

In the present study, the effects of large-scale ($k_s^+ \approx 100$) periodic surface roughness on a high-speed ($M = 2.86$), high Reynolds number ($Re_\theta \approx 60,000$), supersonic turbulent boundary layer was examined. Two roughness topologies (square- and diamond-shaped roughness elements) were compared with an aerodynamically smooth wall. The square roughness model was designed to produce enhanced momentum loss without strong localized pressure gradients. The diamond roughness model, on the other hand, was designed to produce large localized distortions. The measurements included planar contours of the mean and fluctuating velocity, pitot pressure profiles, pressure-sensitive paint, and schlieren photography. The velocity fields over individual elements were resolved in the present study.

For the square roughness model, the schlieren and pressure-sensitive paint results showed that the roughness elements did not produce large localized flow disturbances. The velocity profiles for both the smooth and square roughness models followed the scaling, and the measured local distortion was found to be mild at -0.01. The dominant production terms for both cases were the axial production term P_{xx} and the turbulent-shear-stress production term P_{xy}. The transverse turbulent-stress term P_{yy} was an order of magnitude lower than the other two. For the square roughness, an alternating pattern with a wavelength similar to the roughness spacing was discernible in the extra production. For this roughness topology, most of the production occurred in the bottom 30% of the boundary layer. The turbulence levels were significantly amplified by the roughness; for example, the Reynolds shear stresses were a factor of 2.4 higher than the corresponding smooth-wall values at $y/\delta = 0.3$. These results show that if roughness-induced localized distortions are weak, then inner-scaling captures the main effects of the roughness.

For the diamond roughness model, the schlieren and PSP results showed a pattern of oblique shock and expansion waves, which were generated by the roughness elements. The imposed local distortions were found to have a significant effect on the mean and turbulent flow structure across the entire boundary layer. The transverse velocity V/U_{ref} varied by $\pm 3.0\%$, and the measured distortions were strong, varying from -0.3 to 0.4 across the individual roughness elements. The alternating velocity gradients created production fields that produced and subsequently destroyed the turbulent stresses. Production components that contained the primary velocity gradient remained large. However, the extra alternating production was significant, including the P_{yy} component. Moreover, the extra production was complementary in nature, and the sign and magnitude of the components of the axial and transverse turbulent-stress production terms occurred at the same location. The turbulence levels were found to strongly and rapidly (spatially) respond to the strong localized production; for example, the turbulent shear stresses varied by approximately 100%, traversing from the leading to the trailing edge of a roughness element. These results demonstrated that the strong localized distortions significantly altered the character of the flow, which provided a mechanism for localized manipulation of turbulence in supersonic boundary layers.

Acknowledgments

This work was sponsored in part by the U.S. Air Force Office of Scientific Research under grant/contract number F49620-02-1-0365. The views and conclusions contained herein are those of the authors and should not be interpreted as necessarily representing the official policies or endorsements, either expressed or implied, of the U.S. Air Force Office of Scientific Research or the U.S. Government. The authors also gratefully acknowledge Jorge Martinez and William Seward for their support with wind-tunnel and model construction.

References

[1] Nikuradse, J., "Stromungsgesetze in Rauhen Rohren," *Forschung auf dem Gebiete des Ingenieurwesens*, No. 361, Verein Deutscher Ingenieure, Berlin, July–Aug. 1933; also "Laws of Flow in Rough Pipes," NACA TM 1292, Nov. 1950.

[2] Corrsin, S., and Kistler, A., "Free-Stream Boundaries of Turbulent Flow," NACA Report 1244, 1955.

[3] Perry, A. E., Schofield, W. H., and Joubert, P. N., "Rough Wall Turbulent Boundary Layers," *Journal of Fluid Mechanics*, Vol. 37, 1969, pp. 383–413. doi:10.1017/S0022112069000619

[4] Ligrani, P., and Moffat, R., "Structure of Transitionally Rough and Fully Rough Turbulent Boundary Layers," *Journal of Fluid Mechanics*, Vol. 162, Jan. 1986, pp. 69–98. doi:10.1017/S0022112086001933

[5] Bons, J., Taylor, R., McClain, S., and Rivir, R., "The Many Faces of Turbine Surface Roughness," *Journal of Turbomachinery*, Vol. 123, No. 4, Oct. 2001, pp. 739–748. doi:10.1115/1.1400115

[6] George, J., and Simpson, R., "Some Effects of Sparsely Distributed Three-Dimensional Roughness Elements on Two-Dimensional Turbulent Boundary Layers," AIAA Paper 2000-0915, Jan. 2000.

[7] Antonia, R. A., and Wood, D. H., "Calculation of Turbulent Boundary Layer Downstream of a Small Step Change in Surface Roughness," *Aeronautical Quarterly*, Vol. 26, Aug. 1975, pp. 202–210.

[8] Schlichting, H., *Boundary-Layer Theory*, Springer, New York, 2003.

[9] Wilcox, D. C., *Turbulence Modeling for CFD*, DCW Industries, La Cãnada, CA, 1994.

[10] Grass, A. J., "Structural Features of Turbulent Flow over Smooth and Rough Boundaries," *Journal of Fluid Mechanics*, Vol. 50, 1971, pp. 233–255. doi:10.1017/S0022112071002556

[11] Goddard, F., "Effects of Uniformly Distributed Roughness on Turbulent Skin-Friction Drag at Supersonic Speeds," *Journal of the Aero/Space Sciences*, Vol. 26, No. 1, 1959, pp. 1–24.

[12] Berg, D., "Surface Roughness Effect on a Mach 6 Turbulent Boundary Layer," *AIAA Journal*, Vol. 17, No. 9, 1979, pp. 929, 930.

[13] Liepmann, H., and Goddard, F., "Note on Mach Number Effect upon the Skin Friction of Rough Surfaces," *Journal of the Aero/Space Sciences*, Vol. 23, No. 10, 1957, p. 784.

[14] Young, F., "Experimental Investigation of the Effects of Surface Roughness on Compressible Turbulent Boundary Layer Skin Friction and Heat Transfer," Defense Research Lab., Univ. of Texas Rept. DLR-532, Austin, TX, May 1965.

[15] Latin, R., and Bowersox, R., "Temporal Turbulent Flow Structure for Supersonic Rough-Wall Boundary Layers," *AIAA Journal*, Vol. 40, No. 5, 2002, pp. 832–841.

[16] Bradshaw, P., "The Effect of Mean Compression or Dilatation on the Turbulence Structure of Supersonic Boundary Layers," *Journal of Fluid Mechanics*, Vol. 63, No. 3, 1974, pp. 449–464. doi:10.1017/S0022112074001728

[17] Donovan, J., Spina, E., and Smits, A., "The Structure of Supersonic Turbulent Boundary Layers Subjected to Concave Surface Curvature," *Journal of Fluid Mechanics*, Vol. 259, 1994, pp. 1–24. doi:10.1017/S0022112094000017

[18] Dussauge, J. P., and Gaviglio, J., "The Rapid Expansion of a Supersonic Turbulent Flow—Role of Bulk Dilatation," *Journal of Fluid Mechanics*, Vol. 174, Jan. 1987, pp. 81–112. doi:10.1017/S0022112087000053

[19] Smith, D., and Smits, A., "The Rapid Expansion of a Turbulent Boundary Layer in a Supersonic Flow," *Theoretical and Computational Fluid Dynamics*, Vol. 2, Nos. 5–6, 1991, pp. 319–328. doi:10.1007/BF00271471

[20] Luker, J., Bowersox, R., and Buter, T., "Influence of a Curvature Driven Favorable Pressure Gradient on a Supersonic Turbulent Boundary Layer," *AIAA Journal*, Vol. 38, No. 38, Aug. 2000, pp. 1351–1359.

[21] Arnette, S. A., Samimy, M., and Elliott, G. S., "The Effects of Expansion Regions on the Turbulence Structure of Compressible Boundary Layers," AIAA Paper 96-0656, Jan. 1996.

[22] Bowersox, R., Wier, R., Glawe, D., and Gogineni, S., "Measurements of Turbulent Flow Structure in Supersonic Curved Wall Boundary Layers," *Journal of Propulsion and Power*, Vol. 16, No. 1, 2000, pp. 153–154.

[23] Bowersox, R., and Buter, T., "Mass-Weighted Turbulence Measurements in a Mach 2.9 Boundary Layer with Mild Adverse and Favorable Pressure Gradient," *AIAA Journal*, Vol. 34, No. 12, 1996, pp. 2470–2483.

[24] Latin, R., and Bowersox, R., "Flow Properties of a Supersonic Boundary Layer with Wall Roughness," *AIAA Journal*, Vol. 38, No. 10, 2000, pp. 1804–1821.

[25] Liu, T., and Sullivan, J. P., *Pressure and Temperature Sensitive Paints*, Springer–Verlag, Berlin, 2005.

[26] Navarra, K. R., Rabe, D. C., Fonov, S. D., Goss, L. P., and Hah, C., "The Application of Pressure- and Temperature-Sensitive Paints to an Advanced Compressor," *Journal of Turbomachinery*, Vol. 123, No. 4, 2001, pp. 823–829. doi:10.1115/1.1400116

[27] Adrian, R., *Bibliography of Particle Velocimetry Using Imaging Methods: 1917–1995*, TSI, St. Paul, MN, 1996.

[28] Bowersox, R., "Combined Laser Doppler Velocimetry and Cross-Wire Anemometry Analysis for Supersonic Turbulent Flow," *AIAA Journal*, Vol. 34, No. 11, 1996, pp. 2269–2275.

[29] dPIV, 32-Bit PIV Analysis Code, Software Package, Ver. 2.1, Innovative Scientific Solutions, Dayton, OH, 2005.

[30] Benedict, L. H., and Gould, R. D., "Towards Better Uncertainty Estimates for Turbulence Statistics," *Experiments in Fluids*, Vol. 22, No. 2, 1996, pp. 129–136. doi:10.1007/s003480050030

[31] Reynolds, R., Hayden, I., Castrol, P., and Robins, A., "Spanwise Variations in Nominally Two-Dimensional Rough-Wall Boundary Layers," *Experiments in Fluids*, Vol. 42, No. 2, Feb. 2007, pp. 311–320. doi:10.1007/s00348-006-0243-5

[32] Townsend, A., *The Structure of Turbulent Shear Flow*, 2nd ed., Cambridge Univ. Press, Cambridge, England, U.K., 1976.

[33] Klebanoff, P., "Characteristics of Turbulence in a Boundary Layer with Zero Pressure Gradient," National Committee for Aeronautics, Rept. 1247, May 1954; also NASA TN 3178, 1954.

[34] Van Driest, E. R., "Turbulent Boundary Layer in Compressible Fluids," *Journal of the Aero/Space Sciences*, Vol. 18, No. 3, 1951pp. 145–160.

[35] White, F., *Viscous Fluid Flow*, McGraw–Hill, New York, 2006.

[36] Schetz, J. A., *Boundary Layer Analysis*, Prentice–Hall, Englewood Cliffs, NJ, 1993.

N. Chokani
Associate Editor